On the Sherwood number correction due to Stefan flow

(article starts on next page)

On the Sherwood number correction due to Stefan flow

Maulana G. Nugraha, Ronnie Andersson *, Bengt Andersson
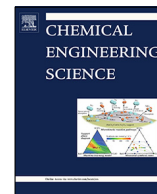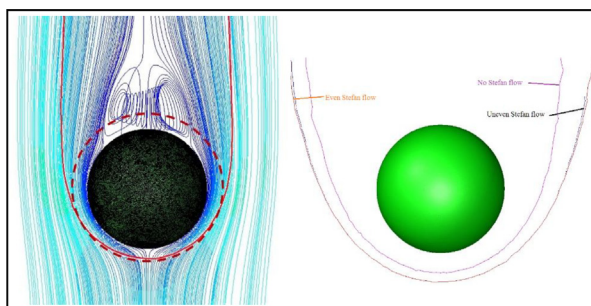
Department of Chemistry and Chemical Engineering, Chalmers University of Technology, SE-41296 Gothenburg, Sweden

HIGHLIGHTS

- Detailed analysis of mass transfer to spheres using CFD analysis.
- Analytical formulation of Stefan flow effect on the mass transfer.
- Accurate Sherwood number models for systems influenced by Stefan flow.

GRAPHICAL ABSTRACT

ARTICLE INFO

ABSTRACT

This study contributes with insight and new models for mass transfer to spheres for three different conditions i.e. mass transfer without Stefan flow, mass transfer with even Stefan flow and mass transfer with uneven flux driven Stefan flow. High resolved computational fluid dynamic simulations of mass transfer without Stefan flow resulted in a new correlation that improves the prediction compared to the model suggested by Ranz-Marshall particularly for higher Sc numbers. A new model for mass transfer which accounts for the convective transport within the 'film' surrounding the particle, and an increase in the film thickness due to the Stefan flow was successfully derived. It is concluded that the new model provides improved accuracy compared to the Spalding and Abrahamzon models and that the relative error for the Sherwood number can be reduced by about half.

1. Introduction

Empirical models for Sherwood number without net boundary layer flow (i.e. without Stefan flow or blowing) are established since more than 60 years. The most frequently used models are the Sherwood number correlations proposed by Frössling and Ranz-Marshall (Frössling, 1938; Ranz and Marshall, 1952). These models are empirical correlations based on the same dimensionless numbers, but they predict different Sherwood numbers for the same Reynolds and Schmidt numbers. The empirical data from earlier time scatter and the exact experimental conditions also differ which explain the difference between the models. A more

recent model was presented by Clift et al (Clift et al., 1978). Different kind of evaporation experiments were the most commonly used methods to study mass and heat transfer rates in the first reported models (Frössling, 1938; Ranz and Marshall, 1952) and in later articles (Sazhin, 2006; Sazhin, 2017). These conditions limit the study to heat transfer to the particle combined with mass transfer from the surface at steady state. Experiments at low vapor pressure reduces the problem with net boundary layer flow, i.e. reduces the Stefan flow. However, the observed Sherwood number will model a combined transport of heat to and mass from the surface. Some computational fluid dynamic (CFD) simulations focusing on the shape and internal recirculation within droplets (Feng and Michaelides, 2000) and for a wide range of Peclet numbers in the creeping flow regime (Frankel and Acrivos, 1968; Kovatcheva et al., 1993) have also been reported.

* Corresponding author.
  E-mail address: ronnie.andersson@chalmers.se (R. Andersson).

Nomenclature

A	Area [m^2]
An	Andersson number $u_s d/D$ [-]
b	Coefficient for Sherwood number correlation without Stefan flow [-]
B_M	Spalding number for Sherwood number due to Stefan flow [-]
B_T	Spalding number for Nusselt number due to Stefan flow [-]
C	Concentration [kg m^{-3}]
Cp	Heat capacity [J kg^{-1} K^{-1}]
d	Particle diameter [m]
D	Diffusivity [m^2 s^{-1}]
F_M	Film thickness correction [-]
k_c	Mass transfer rate coefficient [m s^{-1}]
Le	Lewis number [-]
$\dot{m}$	Total vapor flux [kg s^{-1}]
N	Flux at the surface [kg m^{-2} s^{-1}]
Nu	Nusselt number [-]
r	Local radius [m]
R	Radius [m]
Re	Reynolds number [-]
Sh	Sherwood number [-]
Sc	Schmidt number [-]
u	Stefan flow [m s^{-1}]

U	Bulk velocity [m s^{-1}]
x	Dimensionless space variable [-]
Y	Mass fraction of evaporated species [kg kg^{-1}]

Greek letters

α	Model parameter Film thickness of mass transfer [m]
δ_M	
δ_T	Film thickness of heat transfer [m]
μ	Viscosity [kg m^{-1} s^{-1}]
ρ	Density [kg m^{-3}]
φ	Properties correction factor

Subscripts

0	Original, without Stefan flow
CFD	CFD simulation result
adj	Adjusted
b	Boundary layer
g	Bulk gas
s	Surface
v	Evaporated species
$v\infty$	Evaporated species at infinite location
vs	Evaporated species at surface

Evaporation of gases from particles and droplets have a large effect on the rate of mass and heat transfer. The flow out from the particles or droplets adds a convective transport and in addition it affects the diffusional transport in the mass transfer film surrounding the particle. Most models are based on a steady state approximation of mass and heat transfer and give a direct correlation between the heat transfer and the Stefan flow (Sazhin, 2006; Sazhin, 2017; Spalding, 1979; Miller et al., 1998). In these models the evaporated gas is transported away from the drop with the Stefan flow and heat is transported to the droplet against the Stefan flow. In many cases the droplets or particles are heated from the surrounding gas and these experimental limitations lead to an uneven heating and difficulties in developing a theoretical understanding.

Not only droplet evaporation involves Stefan flow. Devolatilization of biomass also involves mass transfer and convective and radiative heat transfer. These models do not involve direct coupling between mass and heat transfer rates since the heat transferred to the particle is needed both for interior heat conduction and pyrolysis of the solid material resulting in a time delay between heating and evaporation. The experimental techniques (Borodulin et al., 2017; Galgano et al., 2018) as well as the modeling will differ somewhat from evaporation of droplets (Kuznetsov and Strizhak, 2010; Remacha et al., 2018).

Today, complex transport phenomena are studied by numerical simulations e.g. using CFD analyses. CFD analysis provides information about the entire flow field and species concentration which means that the influence of the Stefan flow can be analyzed and quantified accurately. When the mass flow at the particle surface is known it is possible to formulate a model for mass and heat transfer rate that corrects the nominal Sherwood and Nusselt numbers. This study presents CFD simulation that improves the understanding, and it proposes a model that is also suitable for transient simulations since it only requires steady state in the mass transfer film but does not require a steady state balance between heat and mass transfer for the particle. The objective of this study is therefore to describe the effect of Stefan flow as a correction to the nom-

inal Sherwood number, Sh_0, i.e. the Sherwood number without Stefan flow that can easily be embedded in single particle models to predict the correct mass transfer rate.

In this study, three different cases are investigated i.e. mass transfer without Stefan flow, mass transfer with even Stefan flow and mass transfer with uneven Stefan flow e.g. originating from convective heating from a surrounding gas flow. Any significant difference in diffusional transport to and from the surface are also analyzed in the current work.

2. Models for mass transfer

The mass transfer rate to and from surfaces in systems without Stefan flow are traditionally modeled using the film theory by using correlations for the Sherwood number. These models assume constant surface concentration, and a stagnant film with a uniform and fixed thickness related to the Reynolds and Schmidt numbers. The most common models are model in Eq. (1) by Frössling (1938), in Eq. (2) by Ranz and Marshall (1952) based on experiments and in Eq. (3) from a compilation of several numerical simulations by Clift et al. (1978).

$$Sh_0 = 2 + 0.522Re^{1/2}Sc^{1/3} \quad Re < 150 \quad 0.5 < Sc < 2 \tag{1}$$

$$Sh_0 = 2 + 0.6Re^{1/2}Sc^{1/3} \quad Re < 150 \quad 0.5 < Sc < 2 \tag{2}$$

$$Sh_0 = 1 + (1 + ReSc)^{1/3}f(Re) \quad Re < 400 \quad 0.24 < Sc < 100 \tag{3}$$

where $f(Re) = 1$ for $Re \leqslant 1$ and $f(Re) = Re^{0.077}$ for $1 \leqslant Re \leqslant 400$.

Flow around a particle combined with simultaneous mass and heat transfer is a complex phenomenon as illustrated in Fig. 1. However, most models are based on the film theory and assume that the transport only occurs by diffusion through the boundary layer. The film assumption predicts a stagnant film with a thickness of $\delta = d/Sh$ with only molecular diffusion transport. Nevertheless, there is an additional convective transport to the surface as seen in the figure. The empirical models compensate this addi-
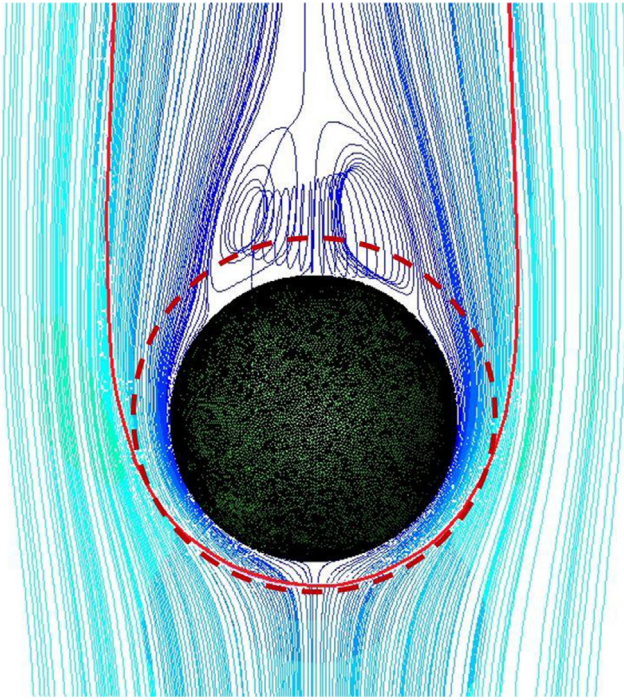
Fig. 1. Streamlines colored by velocity magnitude superposed with *iso*-concentration lines for 0.95 $C_{A,\infty}$ (solid red line), originating from CFD simulation, and the fictitious film thickness according to the film theory for $Sh = 9.15$ (dashed red line). (For interpretation of the references to colour in this figure legend, the reader is referred to the web version of this article.)

tional transport by predicting a film thickness that depends on Reynolds and Schmidt numbers. The theoretical limitations to these models are for a sphere $Sh = 2$ with $Re \rightarrow 0$ and $Sc^{1/3}$ for high Pe numbers. However, $Sc^{0.4}$ is most often observed for lower Peclet numbers, which explains that the Sherwood number correlations found in the literature have a Sc number dependence to the power of 1/3 to 0.4.

Mass transfer due diffusion and convection in the film surrounding a spherical particle influenced by Stefan flow can be written as (assuming constant density)

$$D\left(\frac{1}{r^2}\frac{d}{dr}r^2\frac{dC}{dr}\right) - u\frac{dC}{dr} = 0 \tag{4}$$

Many authors have presented an analytical solution to Eq. (4) e.g. Spalding (1979); Sazhin (2006) and Tonini and Cossali (2015, 2016). However, the boundaries in the bulk are only known for a stagnant particle and for convective transport we must rely on empirical Sherwood number correlations or simulated data.

There are several models proposed for single component evaporation based on the Spalding numbers for mass and heat transfer B_M and B_T. In these models, the Sherwood number is corrected with a function that includes the mass fraction of evaporated species at the surface and in the bulk respectively. An empirical correlation is suggested by Michaelides, 2006

$$Sh = \left[2 + 0.87Re^{1/2}Sc^{1/3}\right]/(1+B_M)^{0.7} \tag{5}$$

where $B_M = \frac{Y_{vs} - Y_{v\infty}}{1 - Y_{vs}}$.

The Sherwood number may also be estimated from a function of the Sherwood number without Stefan flow, Sh_0, as in the original Stefan-Fuchs model and also shown by Spalding (1979).

$$Sh = \frac{\ln(1+B_M)}{B_M}Sh_0 \tag{6}$$

For heat transfer, the Nusselt number is correlated in a similar manner to account for the Stefan flow,

$$Nu = \frac{\ln(1+B_T)}{B_T}Nu_0 \tag{7}$$

here $B_T = (1+B_M)^\varphi - 1$ and $\varphi = \left(\frac{c_{pv}}{c_{pg}}\right)\frac{1}{Le}$.

If the specific heat capacity of the evaporating compounds and the gas are equal and the Lewis number equals unity the Spalding heat transfer number is reduced to $B_T = B_M$.

The Abrahamzon and Sirignano model (Abramzon and Sirignano, 1989) introduces a correction factor to the Spalding model to account for the increase in film thickness, $F_M = \delta_M/\delta_{M0}$ and $F_T = \delta_T/\delta_{T0}$, where the index 0 denotes the film thickness without Stefan flow defined in Eq. (25) in Appendix. Abrahamzon and Sirignano approximated this correction factor to

$$F_M = (1+B_M)^{0.7}\frac{\ln(1+B_M)}{B_M} \tag{8}$$

This leads to an intermediate Sherwood number, Sh^*,

$$Sh^* = 2 + \frac{Sh_0 - 2}{F_M} \tag{9}$$

which is then adjusted due to the Stefan flow in the film, leading to an overall corrected Sherwood number,

$$Sh = Sh^*\frac{\ln(1+B_M)}{B_M} \tag{10}$$

In analogy the corresponding equations for the Nusselt number the B_M value is replaced with B_T. The models above tend to be very complex when a mixture of gases evaporate, and individual components having different diffusivities and vapor pressure also add to the level of complexity (Feng and Michaelides, 2000; Tonini and Cossali, 2016; Ebrahimian et al., 2012; Kryukov et al., 2004).

3. Modeling and analysis

Stefan flow adds a convective transport to or from the particle surface, depending on the net molar flow through the boundary layer. There are two main effects of Stefan flow on the mass and heat transfer rates to particles. Firstly, the convective flow to or from the particle surface will enhance or decrease the transport in the film around the particle. Secondly, the Stefan flow will also affect the thickness of the "stagnant" film around the particle and it may also change the conditions for flow separation occurring at the particle surface. In modeling the effect of Stefan flow, it is required to model the effect of the convective transport and estimate the boundary layer thickness where the concentration or temperature is equal to the bulk concentration or temperature. The Sherwood numbers including the effect of Stefan flow can be obtained from experiments or from detailed high resolved CFD simulations. In order to obtain a simple model, it is required to identify the critical dimensionless numbers that determine the effect of Stefan flow on mass and heat transfer rates. The influence of Stefan flow on transport through the boundary layer of a sphere is given by Eq. (4). The flux from the surface can be separated into diffusional and convective flux at the surface,

$$N = -D\frac{dC}{dr}\Big|_{r=R} + u_sC_s = k_c(C_s - C_b) + u_sC_s \tag{11}$$

An analytical solution of Eq. (4) for one evaporating compound was presented by Spalding (1979) for $Sh = 2$ and for a flat surface by Bird et al., 1960. A more general derivation of the analytical solution is presented in the Appendix which allows us to formulate a simpler dimensionless relationship and also stress the importance of the film thickness.

Correlations are in general easier to handle in dimensionless form and Eq. (4) can be written as

$$\frac{1}{x^2}\frac{d}{dx}x^2\frac{dC}{dx} - \frac{An}{2}\frac{1}{x^2}\frac{dC}{dx} = 0 \tag{12}$$

where $x = r/R$, the dimensionless number An is defined as $An = u_s d/D$. Here u_s is the Stefan flow at the surface. Thereby the solution of Eq. (12) is only a function of the dimensionless number An and the boundary conditions. The derivation of the Sherwood number $Sh = k_c d/D$ is presented in the Appendix.

$$Sh = \frac{An}{e^{\frac{An}{Sh_0}} - 1} \tag{13}$$

This model will only compensate for the convective flow in the film. It is expected that the film will increase in thickness due to the Stefan flow out from the particle. The effect on diffusional mass transfer is illustrated in Fig. 2. Here the solid blue line is the concentration profile without Stefan flow, the dashed red line is illustrates the effect of Stefan flow without adjusted film thickness (Eq. (28) in Appendix) on the concentration profile, and finally the dotted blue the profile shows the results from Eq. (28) while using an adjusted Reynolds number that affect the film thickness via Sh_0 in the equation. The net diffusional mass transfer is given by the gradient at $r/R = 1$ and the diffusivity.

In addition, the flow separation behind the particle will change and for sufficiently high Stefan flow it vanishes completely. A simple empirical adjustment to the model is to calculate a new Sherwood number that takes the Stefan flow effect on film thickness and flow separation into account in addition to the convective transport in the film, by calculating an adjusted Sherwood $Sh_{0,adj} = f(U, u_s, d, \rho, \mu, D)$ and replace Sh_0 with $Sh_{0,adj}$ in Eq. (13). This model is fitted to detailed CFD simulations that spans the interesting range of Re, Sc and An dimensions using non-linear regression analysis. A residual analysis will reveal possible additional effects and determine the valid range for the final model.

4. Computational fluid dynamics simulations

The direct numerical simulations in this study are limited to laminar bulk flow i.e. a bulk Reynolds number $Re < 800$ and low to intermediate particle Reynolds number, Re_p, where the mass and heat transfer is steady. Flow separation and vortex formations
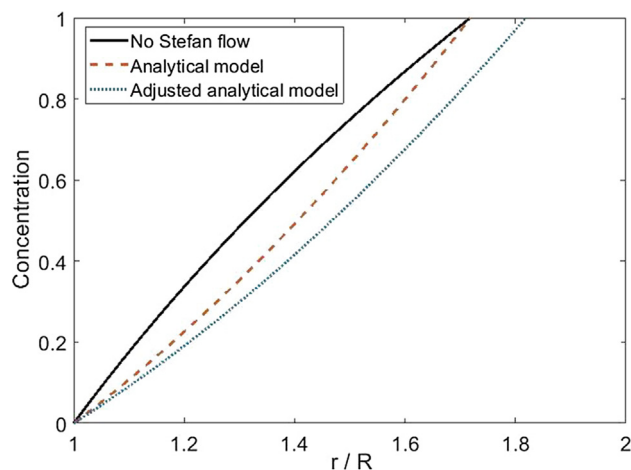

Fig. 2. Concentration profiles in a 'stagnant' film. The solid and the dashed lines show the concentration profiles assuming Stefan flow independent film thickness with and without Stefan flow for a sphere with $Sh_0 = 4.8$ and $An = 2$. The dotted blue line is with an adjusted film thickness that fit the simulated Sh number for $An = 2$. (For interpretation of the references to colour in this figure legend, the reader is referred to the web version of this article.)

behind particles start already at $Re_p = 20$. These vortices begin to shred around $Re_p = 150$ for spheres resulting in time dependent mass transfer and Sherwood number. At higher particle Reynolds number, the flow becomes random and considered turbulent. For this reason, the present study is limited to the flow regime $Re_p < 150$ similar to the regime where empirical correlations are defined. The particle is modelled as a thin porous hollow sphere using two different particles diameters $d_0 = 1$ mm and 10 mm respectively. The porous layer thickness with a very dense mesh is defined as $0.01d_0$. The flux of the different compounds is more accurately calculated by integration of the reactions in the porous layer than from the net transport between outflow and inflow as shown in Eq. (14) below.

In order to analyze mass transfer without Stefan flow and validate the accuracy of the numerical simulations a very fast irreversible reaction $A \rightarrow A^*$ is allowed to occur in the porous layer using identical fluid properties for components A and A^*. Since the reaction is very fast the concentration in the particle is zero everywhere except on the particle surface, i.e. the estimated Sherwood number will be the Sherwood number for constant surface concentration. The stoichiometry $A \rightarrow A^*$ eliminates a net flow due to the reaction. A third component A^{**} with identical fluid properties is defined as constant very low concentration in the particle to analyze the difference between transport to and from the surface with and without Stefan flow. Using three identical compound makes it possible to identify when a converged solution is reached and the same Sherwood number is obtained for flow to and from the surface at steady state.

Simulations for even Stefan flow are done for a range of Stefan flows, where the source for the Stefan flow is introduced in the CFD analysis in two ways, as a mass source in the thin porous layer and a mass flow of a component B entering on the inner surface of the thin porous layer. This will give the same Stefan flow rate in all directions and correspond to a particle with equal heating on the whole surface e.g. by heat radiation for a particle with high heat conductivity or a droplet with large internal recirculation. Uneven Stefan flow is simulated using a source for Stefan flow that is set proportional to the mass transfer to the particle. This will simulate the convective heating and Stefan flow where the particle is heated from the gas flowing around the particle.

The simulation domain is cubic with sides 20 times the particle radius i.e. large enough to allow insignificant increase in velocity around the particle due to the presence of the walls. The computational meshes are made very fine and regular in the boundary layer. The boundary conditions for the inlet flow is defined as velocity boundary condition and the outlet flow is defined as outflow. The exterior walls are defined using a free-slip condition and a very high flow resistance was defined for the porous surface i.e. a no-slip condition is defined for the particle surface. Mesh independence tests were done using local mesh adaption based on the gradients of the solutions variables to ensure that the solution is indeed mesh independent.

In the proceeding data analysis, the mass transfer rate is calculated from the molar flow of A^*, A^{**} and B at the outlet. The accuracy of the numerical simulations is also confirmed by comparing the net balance of component A, and by integrating the reaction rate in the hollow porous sphere. Thereby three relationships defined by Eq. (14) are used to confirm the consistency of the simulation results. In Eq. (14) the inflow and outflow are defined in the y-direction.

$$Flux = \int_{A_{out}} U_y C_{A^*} dA = \int_{A_{in}} U_y C_{Ain} dA - \int_{A_{out}} U_y C_A dA$$

$$= \int_{V_{particle}} r_A dV \; [\text{mol/s}] \tag{14}$$

The flux of B is obtained directly from the defined boundary condition. Given the flux of the species the calculation of the Sherwood number is done based on the classical film theory i.e. an average surface concentration C_s and a constant bulk concentration C_b far from the surface.

$$Sh = \frac{(Flux/A_{particle} - u_s C_s)d}{D \cdot (C_b - C_s)} \tag{15}$$

The flux and corresponding Sherwood number for the main evaporating species B and the third component A** is calculated in the same way. The Stefan flow is calculated from the net mass increase in the system

$$\dot{m} = \int_{A_{out}} U_y \rho dA - \int_{A_{in}} U_y \rho dA \qquad [kg/s] \tag{16}$$

which allows the velocity at the surface u_s to be calculated from $\dot{m}$ and the density. Surface integration of the flux using the definitions in Eq. (14) and integration of the reaction rate, converged to the same number with 4 digits accuracy. Thereby the Sherwood number calculations have very low numerical error.

The continuity, momentum and species balance equations were discretized using second-order accurate schemes, and the pressure–velocity coupling was handled using the SIMPLE algorithm (Andersson et al., 2011). The governing equations were solved using a segregated solver approach with ANSYS Fluent 19.0. A high-quality mesh of prism layers in the surface region both on the fluid and the porous body sides were used to minimize numerical diffusion as depicted in Fig. 3. The thickness of the boundary layer is lowest for higher Re number and low An numbers thereby steepest gradients are expected for this condition. Evaluation of mesh independence at this condition therefore allows a conservative test to ensure the results are not mesh dependent. A nominal mesh, 3.3 million cells, was subsequently refined by increasing the number of mesh adaptions in regions with large gradients of species up to 6.3 million cells as seen in Fig. 3. The mesh independence was tested both at low Re numbers below flow separations and at high Re numbers with flow separation when recirculation behind the particle becomes important.

As shown in Fig. 4, the molar fraction profile along a line defined through the middle of the computational domain confirm the mesh independence is reached at 3.3 million cells. The analysis also confirms that mesh independences of the integral mass flux and driving force is reached, since the resulting Sherwood number, calculated from the flux of A* levels out on a steady level at 3.3 million cells. The difference in the Sherwood number at 3.3 M calls and 6.3 M cells is only seen in the fourth digit which means the simulation results are mesh independent.
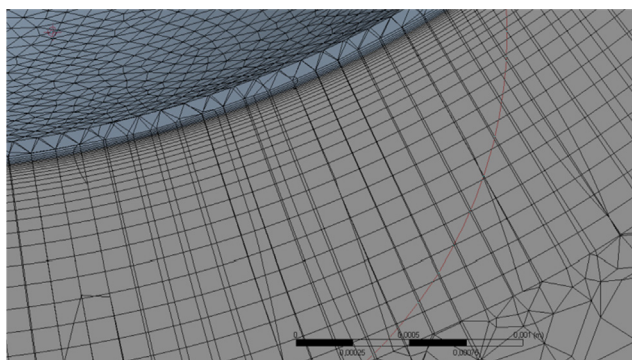

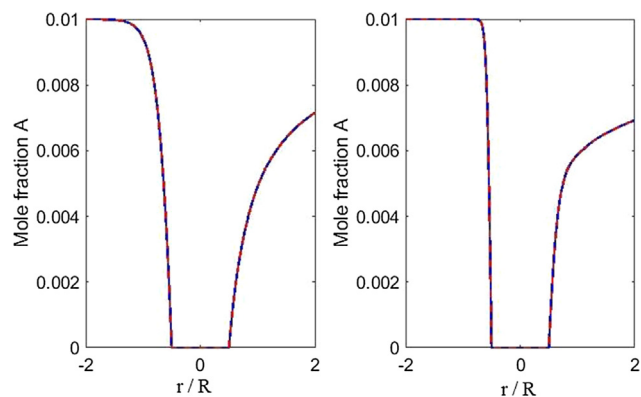**Fig. 3.** Cross section in the computational mesh close to the surface.

Fig. 4. Mesh independence visualized by the concentration profiles in front and behind particle, Solid line low resolution (3.3 M cells) and dashed line high resolution (6.3 M cells) a.) low Re and low Sc and b.) high Re low Sc.

5. Results

5.1. Sherwood numbers without Stefan flow

The simulated data for constant surface concentration and $Re < 150$, $0.5 < Sc < 3$ and for 1 mm and 10 mm particles were fitted to a nonlinear model using 'lsqnonlin' in Matlab.

$$Sh_0 = 2 + b_0 Re^{b_1} Sc^{b_2} \tag{17}$$

Since there are no random errors in the observations it is more important to minimize the relative error of the model than the absolute error, and a minimization of a weighted sum of square was used

$$SS = \left(\frac{Sh_{CFD} - Sh_0}{Sh_0}\right)^2$$

Table 1 summarizes the resulting model parameters and their respective confidence intervals assuming that the residuals between the model predictions and the CFD simulations are random and normal distributed in the logarithmic space. However, since the data are obtained from CFD simulations with insignificant random errors the residuals are in reality lack of fit, but the confidence intervals still give an idea about the accuracy of the model.

This leads to the proposed Sherwood correlation which in traditional form reads,

$$Sh_0 = 2 + 0.486 Re^{0.534} Sc^{0.408} \tag{18}$$

A comparison between the new model and existing models for a wide range of Reynolds and Schmidt numbers reveals that it provides a significantly better fit with the simulated data compared to Ranz-Marshal and Frössling as seen in Figs. 5 and 6. The model by Clift et.al. is more accurate in that it only underpredicts the Sherwood numbers at high Sherwood numbers.

A residual analysis, Fig. 6, shows that the model has no unexplained remaining correlations with the Reynolds or Schmidt numbers. This figure shows the relative error since it is the relative accuracy that is important in the applications. In the simulated

Table 1
Parameters and approximate 95% confidence regions in the model.

	Parameter Eq. (18)	95% confidence
b_0	0.486	0.0051
b_1	0.534	0.0010
b_2	0.408	0.00046
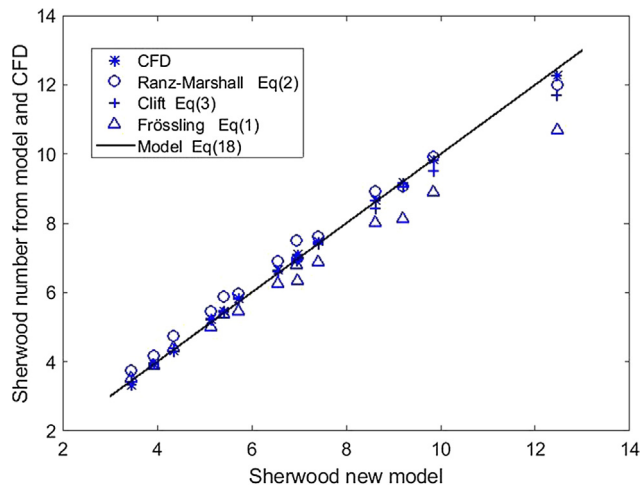
Fig. 5. Comparison between traditional models and the new model (the solid line).

Table 2
Summary of Sherwood number models without Stefan Flow.

Model	Formulation	Relative error range
Present model Eq. (18)	$2 + 0.486Re^{0.534}Sc^{0.408}$	−0.03 to +0.03
Ranz-Marshall Eq. (2)	$2 + 0.6Re^{1/2}Sc^{1/3}$	−0.025 to +0.1
Frössling Eq. (1)	$2 + 0.522Re^{1/2}Sc^{1/3}$	−0.15 to +0.05
Clift Eq. (3)	$1 + (1 + ReSc)^{1/3}f(Re)$	−0.06 to +0.03

data, the model prediction errors are found to always be less than ±3%.

Table 2 summarizes the results from the different models. It is only the model by Clift that is comparable to the present model for the range of *Re* and *Sc* numbers simulated in this study.

5.2. Sherwood number with even Stefan flow

The simplest model for Sherwood number with Stefan flow is given by Eq. (13) assuming only added convective flow and a constant film thickness, and Sh_0 estimated from the new Sh_0 correlation Eq. (18). This model accounts for most of the decrease in *Sh*-number as seen in Fig. 7.

Fig. 7a shows that this simple model fits the data very well even for large reduction of mass transfer due to Stefan flow. However, there are systematic residuals that vary with the *An/Sc* ratio and the Schmidt number as expected since the change in film thickness is not included in the model. This is illustrated in Fig. 8 which shows how the concentration contours around the particle increases with increased Stefan flow.

The correlation for increased film thickness due to Stefan flow suggested by Abrahamzon et al (Abramzon and Sirignano, 1989)

in Eq. (8) gives a too large correction. The residual in Fig. 7 is correlated with $An/Sc = u_s d/v$ which is a Reynolds number and the first approximation is to adjust the Reynolds number in Eq. (18) with the Stefan flow $Re^* = (U - \alpha \cdot u_s)d/v$. The optimal value of $\alpha = 0.3332$ gives the results presented in Fig. 9. The physics behind this model is that the convective transport to the particle from the surrounding flow is decreased by the Stefan flow.

This correction decreases the maximum model residual to below ±6%. There is no overall trend in the residual plot as function of the dimensionless *An/Sc* number, but there is a trend in the *An/Sc* number for different Schmidt numbers as seen in Fig. 9. An improved model, Eq. (19) shown in Fig. 10 removes the trend in *An* and *Sc*.

$$Sh_{0,adj} = 2 + 0.486Re^{0.534}Sc^{0.408} - 0.0576An^{0.49}/Sc^{1.41} \qquad (19)$$

This Sherwood number replaces Sh_0 in Eq. (13). There is still a dependence on *An/Sc* but this dependence is positive for low *Sc* numbers and negative for high *Sc* numbers. However, the residual is below 3% and the accuracy in physical properties and shape of the particles are usually less and there is no reason to develop the model further since the model for Sh_0 has an error in the same range.

A comparison between the new model and traditional models is presented in Table 3. Even the simplest model without any correction for the increased film thickness performs better than the most common models used.

5.3. Multicomponent mass transfer

Multicomponent mass transfer was simulated using the identical compounds A, A* and A** to simulate transport to and from the surface. The different compound B was added to simulate transport in a multicomponent environment of compounds with different proper-
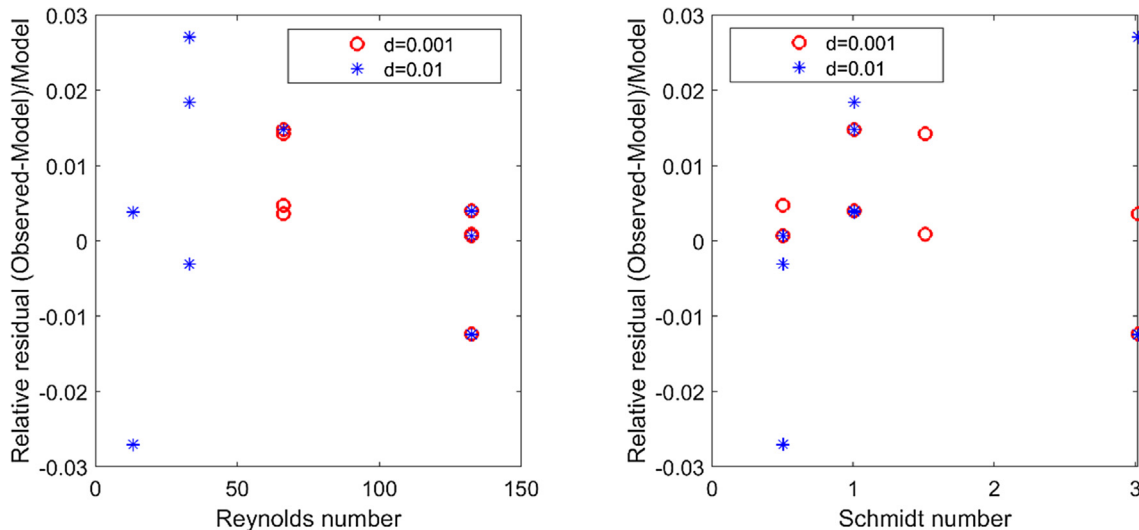

Fig. 6. Residual analysis (CFD simulations-predicted Sh_0 numbers) for the model in Eq. (18) a.) as function of Reynolds number and b.) as function of Schmidt numbers.
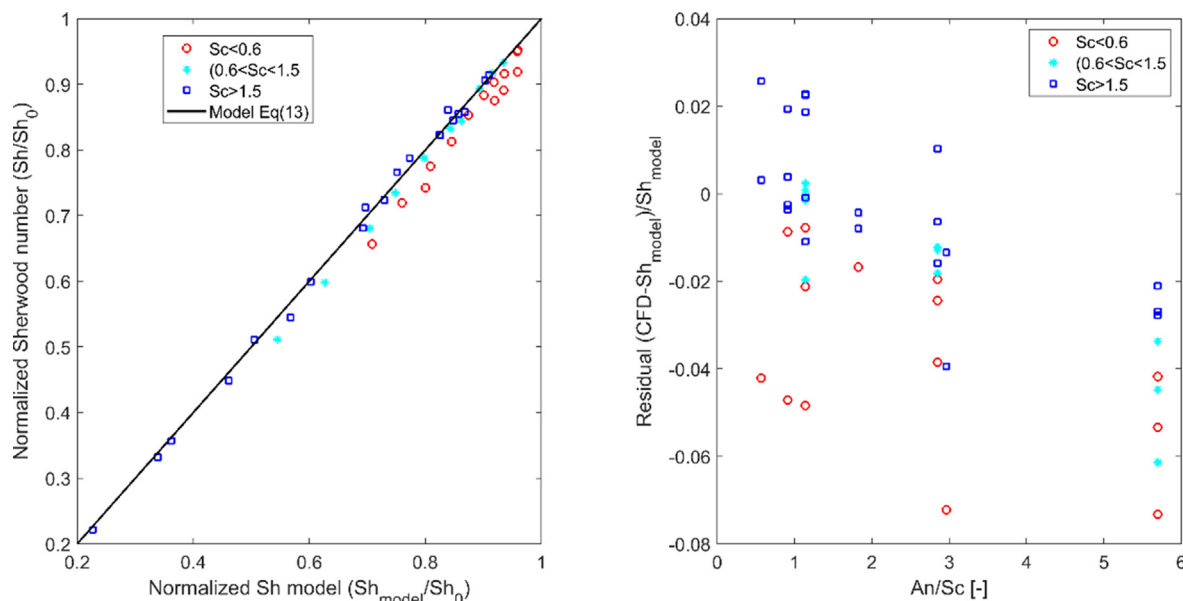
Fig. 7. a.) CFD simulations compared to the analytical model Eq. (13) with Sh_0 Eq. (18) and b.) residual analysis (CFD-Eq. (13)).

ties. The model for Sherwood number formulated in the previous section is implicit and the Sherwood number is obtained from Re and Sc numbers and an iterated net flux at the surface described by the net flow from the surface u_s. The different compounds will have the same u_s but different dimensionless $An = u_s d/D$ number. This iterative procedure allows for multicomponent mass transfer as well as a large variation in net flux. However, the surface concentration is assumed equal on all parts of the surface.

5.4. Sherwood number with uneven flux driven Stefan flow

In the analyses so far, the Stefan flow was uniform around the particle, which correspond to e.g. radiative heating from all sides. However, most of the empirical data on evaporation is generated

from convective heating and the empirical models have been fitted to data with higher evaporation rate upstream on the particle. Assuming local Nusselt numbers equal to local Sherwood numbers, additional simulations with Stefan flow proportional to the mass transfer to the particle were performed in order to compare the traditional empirical models with the proposed models. The direct numerical simulations showed that about 72% ± 3% of the mass transfer to a particle take place at the upstream 50% of the surface. This fraction is not dependent on the Stefan flow described by the An number.

There is only a marginal difference in film thickness between even and uneven Stefan flow as seen in Fig. 8. However, the formulated Sherwood models in Eqs. (13) and (19) do not fit data for uneven vaporization as seen in Fig. 11.
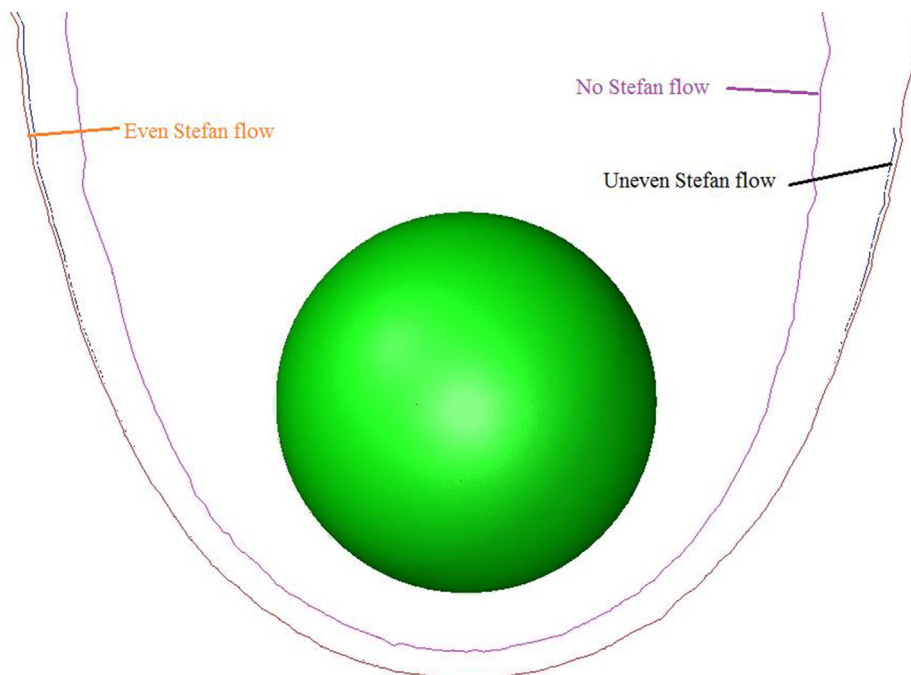

Fig. 8. Contours of concentration of $C_A = 0.95 C_{A\infty}$ with and without Stefan flow at $An = 4.5$.
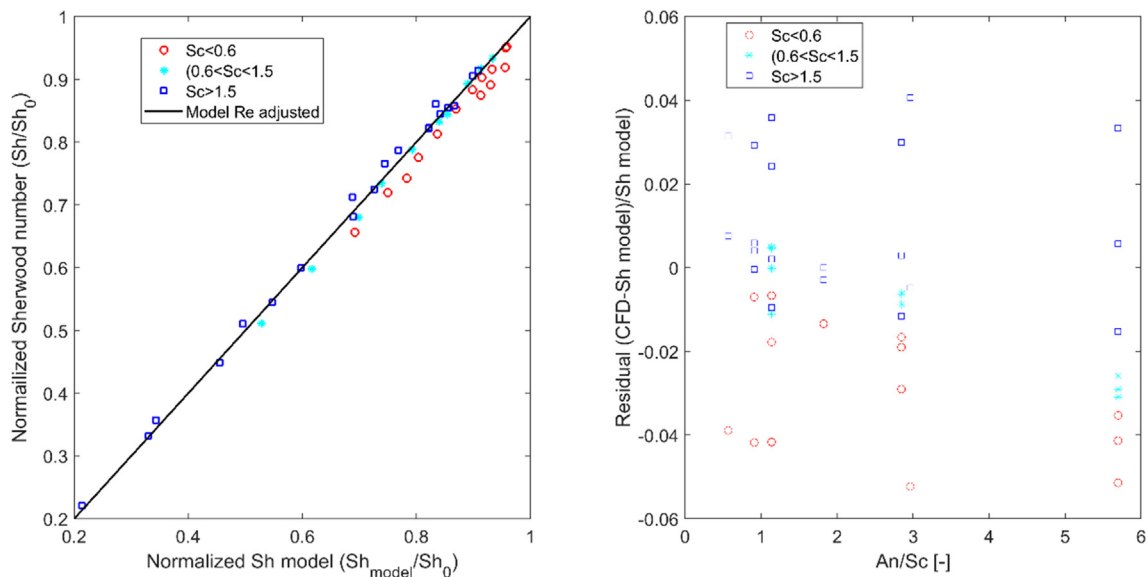
Fig. 9. CFD simulations compared to the analytical model Eq. (13) with Sh_0 calculated from the new Sh_0 model Eq. (18) with adjusted *Re number* $Re^* = (U - 0.3332u_s) \cdot d_p / \nu$.
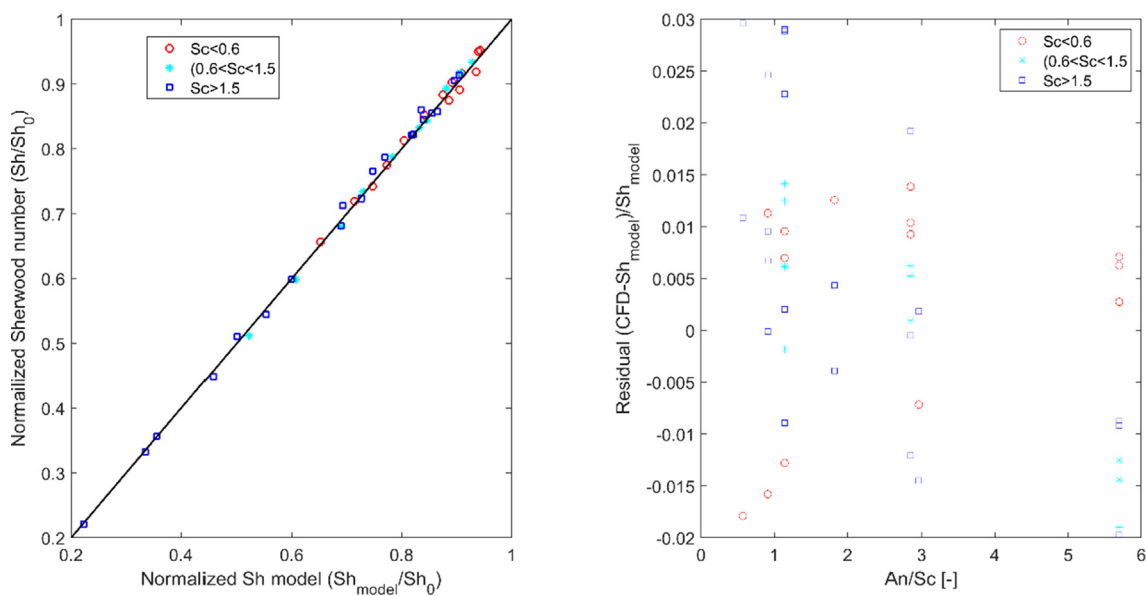

Fig. 10. Final model Eq. (13) with Sh_0 from Eq. (19).

Table 3
Summary of models for Sherwood numbers with even Stefan flow.

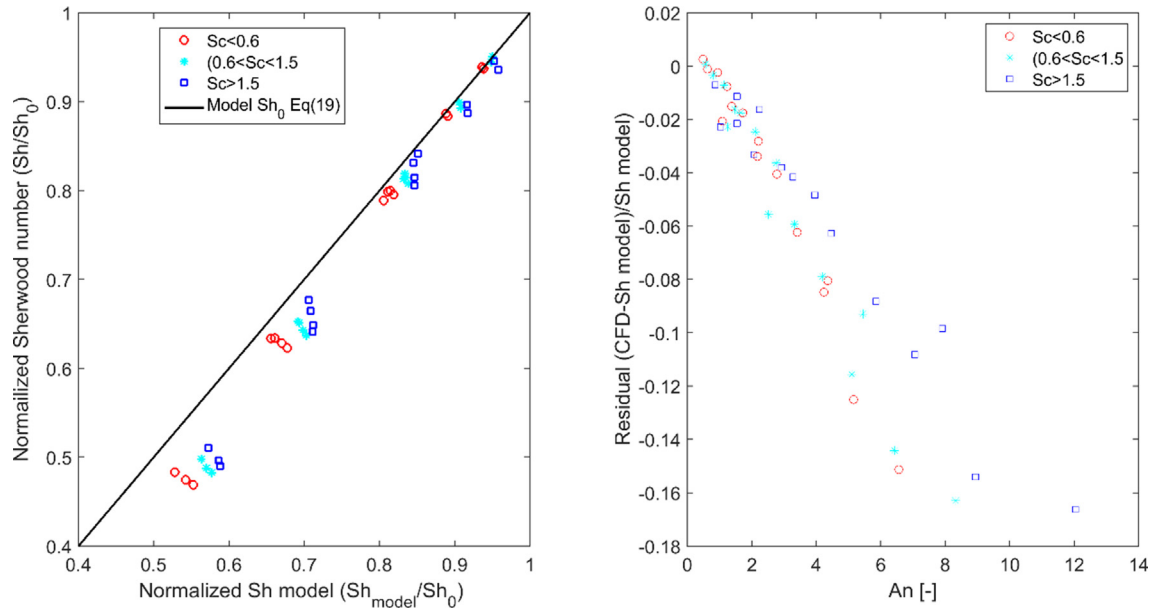| Model	Formulation	Relative error range
Analytical model	$Sh = An / (e^{An/Sh_0} - 1)$	-0.08 to $+0.04$
Adjusted $Re^* = (V - \alpha \cdot u_s) \cdot d / \nu$ $\alpha = 0.333$	$Sh = An / (e^{An/Sh_0(Re^*)} - 1)$	-0.05 to $+0.05$
Adjusted $Sh_{0,adj} = Sh_0 - 0.0576 An^{0.49} / Sc^{1.41}$	$Sh = An / (e^{An/Sh_{0,adj}} - 1)$	-0.02 to $+0.03$
Spalding	$Sh = \frac{\ln(1 - B_M)}{B_M} Sh_0$	-0.12 to $+0.03$
Abrahamzon	Eqs. (8)–(10)	-0.2 to $+0.1$

Fig. 11. The Sherwood model Eq. (13) with Sh_0 from Eq. (19) applied on data for uneven vaporization.

The fraction of mass transfer to the particle that occurs at the upstream half of the particle is about 72% with very little variations due to Schmidt, Reynolds or Andersson number. A simple correction to the model for equal evaporation would be to set the An number higher at the upstream side of the particle. A fraction α of all evaporation will occur at the upstream half of the particle and the surface evaporation velocity as function of the average evaporation velocity $\bar{u}_s$ becomes

$$u_{s,upstream} = \alpha 2\bar{u}_s$$
$$u_{s,downstream} = (1 - \alpha)2\bar{u}_s \tag{20}$$

The total mass transfer is given by

$$Sh = \alpha \cdot Sh(u_{s,upstram}) + (1 - \alpha) \cdot Sh(u_{s,downstream}) \tag{21}$$

This addition to the model decreases the maximum error to below ±9% as shown in Fig. 12. However, a dependence on the An number is still observed. Notably, a better prediction is obtained by using the same structure for Sherwood number correction as in the case for even Stefan flow as shown in Fig. 13.

$$Sh_{0,adj} = 2 + 0.486Re^{0.534}Sc^{0.408} - 0.118An/Sc^{0.25} \tag{22}$$

A comparison between the traditional models with the proposed models are presented in Table 4. In this case, the simplest model without any correction for the increased film is not sufficient. The empirically corrected model by Abrahamzon performs better than for the case with even Stefan flow.
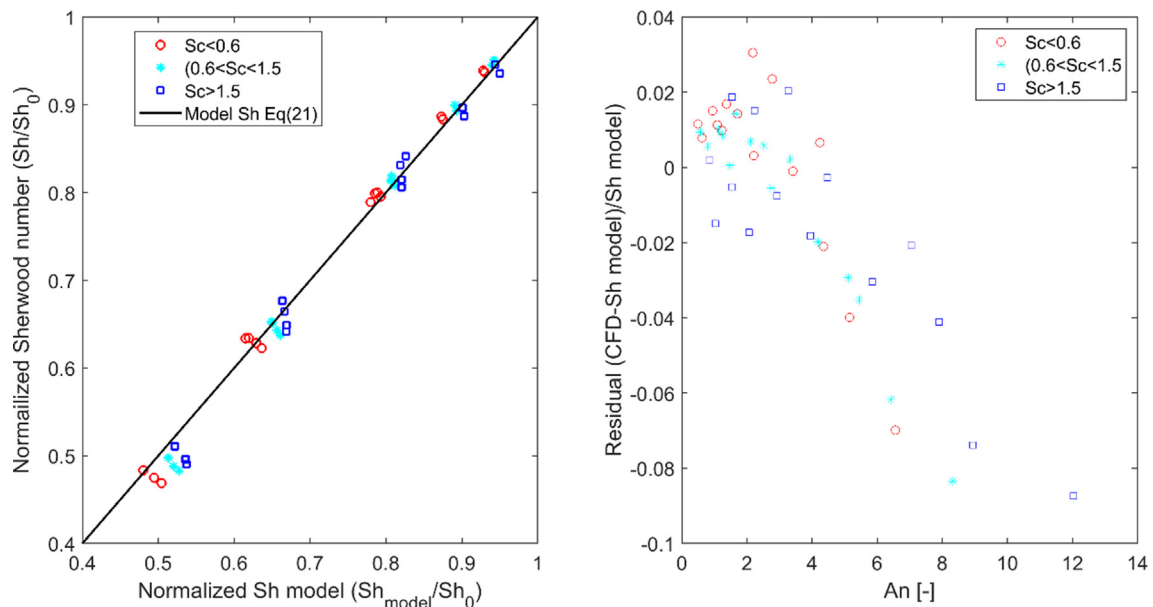

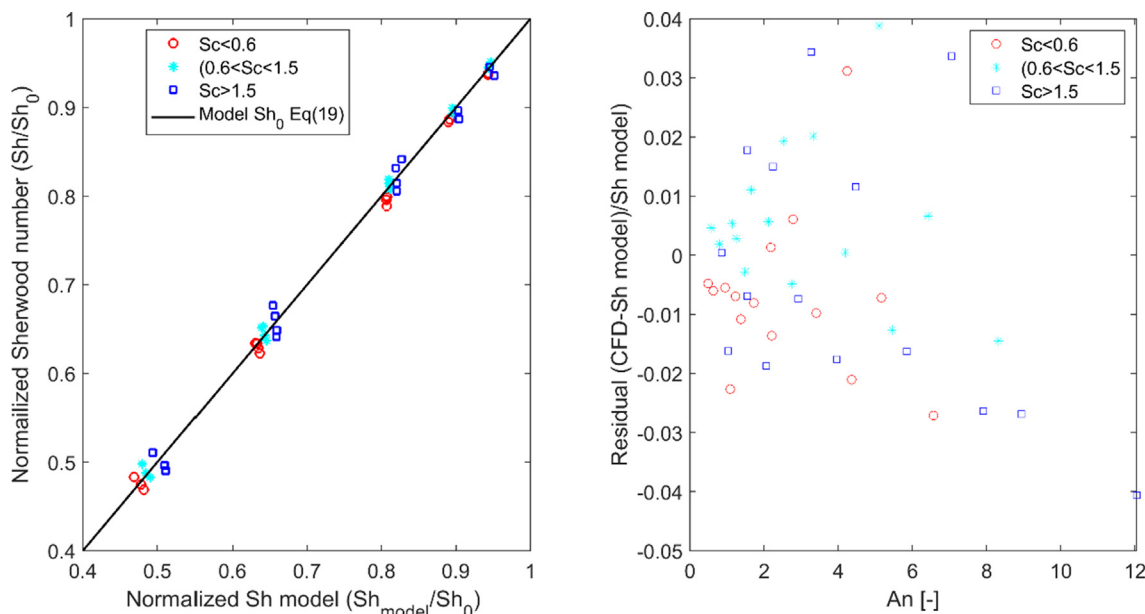**Fig. 12.** The results from model in Eq. (21) with α = 0.72.

Fig. 13. Model Eq. (22) + Eq. (13) for uneven Stefan flow (convective heating).

Table 4
Summary of models for Sherwood numbers with uneven Stefan flow.

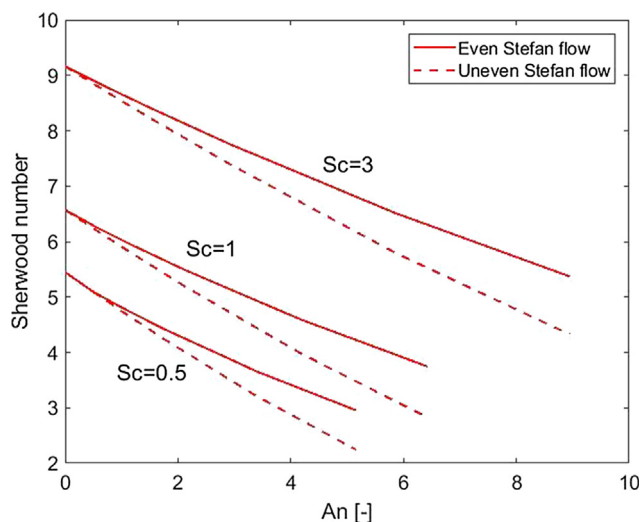| Model	Formulation	Relative error
Analytical model	$Sh = An/(e^{An/Sh_0} - 1)$	0.01–0.22
Weighted	Eq. (13) + Eq. (21)	−0.09 to +0.04
Adjusted $Sh_{0,adj} = Sh_0 - 0.118An/Sc^{0.25}$	$Sh = An/(e^{An/Sh_{0,adj}} - 1)$	−0.04 to +0.04
Spalding	$Sh = \frac{\ln(1-B_M)}{B_M} Sh_0$	0.01–0.15
Abrahamzon	Eqs. (8)–(10)	−0.13 to +0.08

Fig. 14. Comparison between the model predictions for even and uneven Stefan flow at *Re* = 66.

There is a systematic difference in the predicted Sherwood numbers for even and uneven Stefan flow as shown in Fig. 14 where the two models represent the particle with even and uneven Stefan flow.

5.5. Comparison with existing models

Comparison with existing models for evaporation of single compounds are shown in Fig. 15. Existing models have mainly been developed for water evaporation and fit reasonably well for water with *Sc* = 0.66 at 300 K. The difference between convective and equal heating is more pronounced at high *Sc* and *An* numbers as seen in Fig. 15. The traditional models by Spalding and Abrahamzon predicts reasonable Sherwood numbers but do not distinguish between even and uneven heating. Most of the empirical data are for water evaporation and the traditional models are most accurate in predicting Sherwood numbers for low *Sc* numbers close to *Sc* number for water. The empirical model suggested by Michaelides, 2006 gives in general a too high Sherwood number and is not included in Fig. 15.

6. Conclusions

Mass transfer to and from spheres was analyzed and quantified by high resolved CFD simulations for three different conditions i.e. mass transfer without Stefan flow, mass transfer with even Stefan flow and mass transfer with uneven flux driven Stefan flow. The simulations were limited to laminar flow in the range where a steady-state solution exists and covers a range of particle Reynolds numbers, Re_p < 150 and Schmidt numbers 0.5 < *Sc* < 3. The traditional models for mass transfer without Stefan flow, proposed by Frössling (Frössling, 1938) and Ranz and Marshall (Ranz and
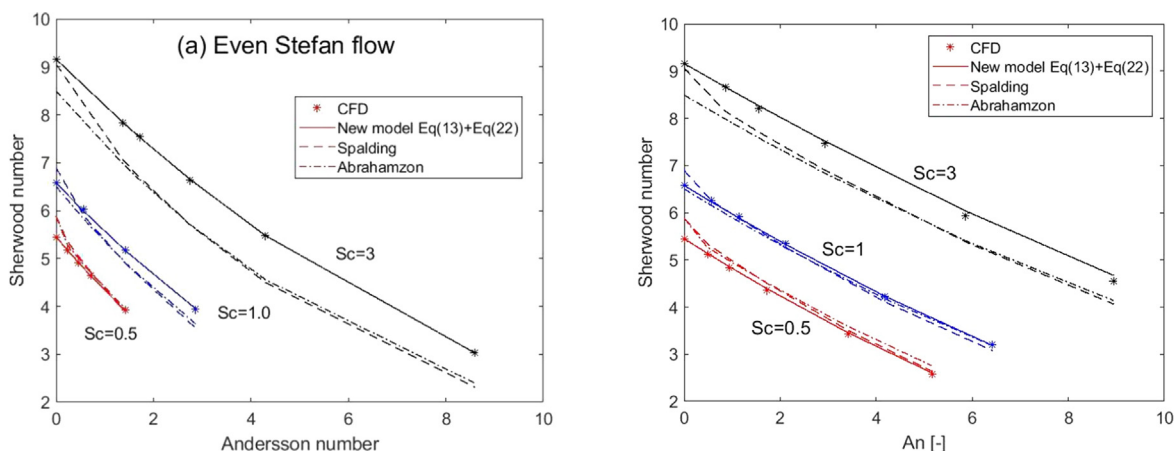
Fig. 15. Comparison between models with (a) even Stefan flow and (b) uneven Stefan flow at *Re* = 66 and different *Sc* numbers.

Marshall, 1952) showed systematic deviation from the CFD simulations while the model by Clift et al (Clift et al., 1978) has a very good fit. The proposed model removes most of the remaining systematic errors and allows improved predictions of mass transfer.

An analysis of the Stefan flow revealed that the rate of mass transfer can be written as a function of the nominal Sherwood number i.e. without Stefan flow and a dimensional number $An = u_s d/D$ and the film thickness. The largest effect of Stefan flow on mass transfer was due to the convective transport within the 'film' surrounding the particle. A minor effect related to an increase in the film thickness due to the Stefan flow could also be inferred from the results. An analytical formulation of the mass transfer rate for a given film thickness assuming spherical symmetry was presented. This model is further refined with an adjusted Reynolds number to account for the increase in film thickness leading to very accurate predictions of the Sherwood number over the entire range of *Re*, *An*, and *Sc* numbers studied. It is concluded that the new model allows significant improvements compared to commonly used models.

The simulations also revealed a systematic difference between even, constant surface concentration, and uneven flux driven Stefan flow due to particles being heated evenly and particles being heated unevenly e.g. from convective heating. A correction of the standard model for mass transfer with convective heating was presented. It is concluded that the new model provides improved accuracy compared to the Spalding and Abrahamzon models and that the relative error for the Sherwood number can be reduced by about half.

CRediT authorship contribution statement

Maulana G. Nugraha: Methodology, Investigation, Validation, Writing – original draft. **Ronnie Andersson:** Conceptualization, Supervision, Writing – review & editing, Project administration, Funding acquisition. **Bengt Andersson:** Conceptualization, Supervision, Writing – review & editing, Funding acquisition.

Declaration of Competing Interest

The authors declare that they have no known competing financial interests or personal relationships that could have appeared to influence the work reported in this paper.

Appendix A

Deduction of a Sherwood number for a sphere including Stefan flow in the mass transfer film.

The convective flow, *u*, depends on the geometry but can be written as a function of the velocity at the surface u_s and radius.

$$u = \frac{u_s R^2}{r^2}$$

In dimensionless form with *x* = *r/R* Eq. (4) becomes

$$\frac{1}{x^2}\frac{d}{dx}x^2\frac{dC}{dx} - \frac{u_s d}{2D}\frac{1}{x^2}\frac{dC}{dx} = 0 \tag{23}$$

By canceling *1/x²* and integrating

$$x^2\frac{dC}{dx} - \frac{An}{2}\cdot C = const \tag{24}$$

This equation describes the flux of evaporation species that is constant in a film surrounding the particle. The solution of Eq. (24) is only a function of the dimensionless number $An = u_s d/D$ and the boundary conditions.

The position of the boundary where $C(x_b) = C_b$ for mass transfer without Stefan flow is obtained by solving Eq. (23) with u_s = 0:

$$x_b = \frac{1}{1 - \frac{2}{Sh_0}} \tag{25}$$

Reformulating Eq. (24) gives

$$\frac{dC}{C - C_s + const \cdot 2/An} = \frac{An}{2}\frac{1}{x^a}dx \tag{26}$$

Eq. (26) has an analytical solution.

$$\ln\left(\frac{C - C_s + const \cdot 2/An}{const \cdot 2/An}\right) = \frac{An}{2}\left(1 - \frac{1}{x}\right)$$

and

$$C = C_s + \frac{2 \cdot const}{An}\left(e^{\frac{An}{2}\left(1 - \frac{1}{x}\right)} - 1\right) \tag{27}$$

Inserting $C = C_b$ at $x = x_b$ and $(1 - 1/x_b) = 2/Sh_0$ from Eq. (25) results in

$$\frac{2 \cdot const}{An} = \frac{C_b - C_s}{e^{An/Sh_0} - 1}$$

We obtain

$$C(x) = C_s + \frac{C_b - C_s}{e^{An/Sh_0} - 1}\left(e^{\frac{An}{2}\left(1 - \frac{1}{x}\right)} - 1\right) \tag{28}$$

The flux at the surface is the sum of diffusional and convective flux

$$N = -D\frac{dC}{dr} + u_s C_s = k_c(C_s - C_b) + u_s C_s \tag{29}$$

Set the diffusional transport in Eq. (29) dimensionless using the analytical derivative of Eq. (28)

$$\frac{dC}{dx} = -\frac{k_c R}{D}(C_s - C_b)$$

$$\frac{An/2}{e^{\frac{An}{Sh_0}} - 1}(C_s - C_b) = \frac{Sh}{2}(C_s - C_b)$$

Finally, the corrected Sherwood number becomes

$$Sh = \frac{An}{e^{\frac{An}{Sh_0}} - 1} \tag{30}$$

References

Abramzon, B., Sirignano, W.A., 1989. Droplet vaporization model for spray combustion calculations. Int. J. Heat Mass Transf. 32 (9), 1605–1618.

Andersson, B., Andersson, R., Håkansson, L., Mortensen, M., Sudiyo, R., Wachem van, B., 2011. Computational Fluid Dynamics for Engineers. Cambridge University Press, Cambridge.

Bird, R.B., Stewart, W.E., Lightfoot, E.N., 1960. Transport Phenomena. John Wiley & Sons, New York.

Borodulin, V.Y., Letushko, V.N., Nizovtsev, M.I., Sterlyagov, A.N., 2017. Determination of parameters of heat and mass transfer in evaporating drops. Int. J. Heat Mass Transf. 109, 609–618.

Clift, R., Grace, J.R., Weber, M.E., 1978. Bubble, Drops, and Particles. Academic Press, New York.

Ebrahimian, V., Nicolle, A., Habchi, C., 2012. Detailed modeling of the evaporation and thermal decomposition of urea-water solution in SCR systems. AIChE J. 58 (7), 1998–2009.

Feng, Z.-G., Michaelides, E.E., 2000. A numerical study on the transient heat transfer from a sphere at high Reynolds and Peclet numbers. Int. J. Heat Mass Transf. 43 (2), 219–229.

Frankel, N.A., Acrivos, A., 1968. Heat and Mass Transfer from Small Spheres and Cylinders Freely Suspended in Shear Flow. Phys. Fluids 11 (9), 1913–2000.

Frössling, N., 1938. The Evaporation of Falling Drops. Gerlands Beitr. Geophys. 52, 107–216.

Galgano, A., Di Blasi, C., De Vita, R., 2018. Experimental Validation of a Solid-Phase Model for Wood Ignition and Burning. Energy Fuels 32 (8), 8494–8506.

Kovatcheva, N.T., Polyanin, A.D., Kurdjumov, V.N., 1993. Mass Transfer from a Particle in Shear-Flow with Surface-Reactions. Acta Mech. 101 (1–4), 155–160.

Kryukov, A.P., Levashov, V.Y., Sazhin, S.S., 2004. Evaporation of diesel fuel droplets: kinetic versus hydrodynamic models. Int. J. Heat Mass Transf. 47 (12-13), 2541–2549.

Kuznetsov, G.V., Strizhak, P.A., 2010. Transient heat and mass transfer at the ignition of vapor and gas mixture by a moving hot particle. Int. J. Heat Mass Transf. 53 (5-6), 923–930.

Michaelides, E., 2006. Particles, bubbles and drops. World Scientific, New Jersey.

Miller, R.S., Harstad, K., Bellan, J., 1998. Evaluation of equilibrium and non-equilibrium evaporation models for many-droplet gas-liquid flow simulations. Int. J. Multiph. Flow 24 (6), 1025–1055.

Ranz, W.E., Marshall, W.R., 1952. Evaporations from Drops 1. Chem. Eng. Prog. 48 (3), 141–146.

Remacha, M.P., Jiménez, S., Ballester, J., 2018. Devolatilization of millimeter-sized biomass particles at high temperatures and heating rates. Part 2: Modeling and validation for thermally-thin and -thick regimes. Fuel 234, 707–722.

Sazhin, S.S., 2006. Advanced models of fuel droplet heating and evaporation. Prog. Energy Combust. Sci. 32 (2), 162–214.

Sazhin, S.S., 2017. Modelling of fuel droplet heating and evaporation: Recent results and unsolved problems. Fuel 196, 69–101.

Spalding, D.B., 1979. Combustion and Mass Transfer. Pergamon Press, Oxford New York.

Tonini, S., Cossali, G.E., 2015. A novel formulation of multi-component drop evaporation models for spray applications. Int. J. Therm. Sci. 89, 245–253.

Tonini, S., Cossali, G.E., 2016. A multi-component drop evaporation model based on analytical solution of Stefan-Maxwell equations. Int. J. Heat Mass Transf. 92, 184–189.